

PROCEEDINGS OF SPIE

SPIDigitalLibrary.org/conference-proceedings-of-spie

Lidar investigations of atmospheric dynamics

C. Russell Philbrick, Hans D. Hallen

C. Russell Philbrick, Hans D. Hallen, "Lidar investigations of atmospheric dynamics," Proc. SPIE 9612, Lidar Remote Sensing for Environmental Monitoring XV, 96120C (1 September 2015); doi: 10.1117/12.2188641

SPIE.

Event: SPIE Optical Engineering + Applications, 2015, San Diego, California, United States

Lidar investigations of atmospheric dynamics

C. Russell Philbrick^{a,b} and Hans D. Hallen^{a*}

^a Physics Department, N.C. State University, Raleigh NC, 27695-8202, USA;

^b MEAS Department, N.C. State University, Raleigh NC, 27695-8208, USA.

ABSTRACT

Ground based lidar techniques using Rayleigh and Raman scattering, differential absorption (DIAL), and supercontinuum sources are capable of providing unique signatures to study dynamical processes in the lower atmosphere. The most useful profile signatures of dynamics in the lower atmosphere are available in profiles of time sequences of water vapor and aerosol optical extinction obtained with Raman and DIAL lidars. Water vapor profiles are used to study the scales and motions of daytime convection cells, residual layer bursts into the planetary boundary layer (PBL), variations in height of the PBL layer, cloud formation and dissipation, scale sizes of gravity waves, turbulent eddies, as well as to study the seldom observed phenomena of Brunt–Väisälä oscillations and undular bore waves. Aerosol optical extinction profiles from Raman lidar provide another tracer of dynamics and motion using sequential profiles atmospheric aerosol extinction, where the aerosol distribution is controlled by dynamic, thermodynamic, and photochemical processes. Raman lidar profiles of temperature describe the stability of the lower atmosphere and measure structure features. Rayleigh lidar can provide backscatter profiles of aerosols in the troposphere, and temperature profiles in the stratosphere and mesosphere, where large gravity waves, stratospheric clouds, and noctilucent clouds are observed. Examples of several dynamical features are selected to illustrate interesting processes observed with Raman lidar. Lidar experiments add to our understanding of physical processes that modify atmospheric structure, initiate turbulence and waves, and describe the relationships between energy sources, atmospheric stability parameters, and the observed dynamics.

Keywords: Raman lidar, atmospheric dynamics, lower atmosphere, waves, turbulence

1. INTRODUCTION

Anyone who looks at the clouds in the summer sky can appreciate the complicity of the many features, large and small, that show the many complex dynamical processes that actively move the clouds about. It seems remarkable to observe the thermodynamic processes that make a cloud grow or shrink, based upon the processes of condensation and evaporation, in the thermal environments existing within an air parcel. However, Earth's atmosphere does enjoy relatively stable conditions, where the solar energy flux input combines with the release of internally stored energy, and the smaller influences from biological processes and man; those inputs are reasonably balanced by the infrared energy radiated from the Earth, together with the backscattered radiation from its surface and from clouds. As energy transfers into and out of the atmosphere, it is governed by optical scattering and absorption of molecules, aerosols, clouds, and by the surface and cloud albedo. The lower 100 km of the atmosphere is turbulently mixed by thermal convection and instabilities created by winds and waves that uniformly mix the photo-chemically stable gases. The Earth's rotation results in dynamical features, which are described as planetary waves and winds that experience Coriolis forces and are forced by orographic features to spawn the large circulation cells, gravity waves, and smaller cells that we observe as the low and high pressure vortices in our weather systems. The winds also generate gravity waves as air flows across orographic features, or form smaller cells and waves of various sizes. Winds across a ridge line force the air to rise, moving the air from its hydrostatic stable condition and resulting in oscillations. Gravity waves are most often an imperceptible micro-baric pressure variation in lower layers of the atmosphere, but as they propagate upward to altitudes of lower pressure, the amplitudes of the temperature and density oscillations increase in proportion to the pressure decrease.

* Further author information: (Send correspondence to C.R.P.)

C.R.P.: E-mail: philbrick@ncsu.edu, Telephone: 919-513-7174

H.D.H.: E-mail: hallen@ncsu.edu, Telephone: 919-515-6314

Gravity waves generally travel great distances because there is little energy dissipation, and they can exhibit relatively large amplitudes in the density and temperature as the atmosphere thins with altitude¹⁻⁹. At an altitude near 90 km, the growth in the amplitude of temperature and density oscillations have increased by a factor of thousands, and temperature wave oscillations greater than 10% are often observed in the mesosphere^{2,3,7,9,10,11}.

Advancements in lasers and detectors during the last few years have opened new opportunities to improve our knowledge of the lower atmosphere properties by profiling the concentrations of the primary chemical species, temperature, aerosol optical extinction, convection, and turbulence, as well as allowing measurements of the microphysical processes that govern cloud formation and phase state changes^{12,13}. Advances have also been made in detecting trace concentrations of chemical species from industrial and power generation air pollution, biogenic processes, and leaks of methane and other gasses from mining, well drilling, fracking, and from buried natural gas pipelines¹⁴. Tunable lasers, laser diodes, and broad band supercontinuum lasers have opened opportunities to make measurements atmospheric composition over a wide range of wavelengths¹⁵⁻¹⁸. These techniques allow measurements of trace level concentrations of chemical species using the unique spectral signatures resulting from optical scattering and absorption of molecules in gas, liquid, and solid phases.

The dynamical processes in the lower atmosphere can be studied by using profiles of water vapor concentration and aerosol optical extinction as tracers of dynamics, and temperature profiles to describe the atmospheric stability^{2,3}. Daytime convection, weather front motion, undular bore waves, and evolution processes of clouds are important features that are studied with Raman lidar¹⁹. The microphysical thermodynamic processes that result in cloud formation can be studied using Raman lidar measurements of temperature and water vapor distribution surrounding cloud formations^{20,21}. Changes in aerosol particle size are observed using multi-wavelength measurements of optical extinction profiles²⁰⁻²⁸. The particle size is also obtained from the ratio of cross-polarized intensities scattered at an angle from the laser beam as the plane of polarization is flipped between parallel and perpendicular to the plane containing the beam and the detectors. The two intensities are then used to form the polarization ratio of the angular variations in the scattering phase function²⁶⁻³¹. The changes in the phase state of water can be studied by comparing the relative amplitudes of the backscattered vibrational Raman signal for the three phase states^{32,33}. These relative variations between the gaseous, liquid and solid phases of water are observed in the Raman spectra by detecting the wavelength shifts in the Raman scatter signature caused by changes in their bond strengths. We expect that it will be possible to quantify both the number density of the liquid and ice particles by combining the Raman lidar measurements and the aerosol size information obtained by using the polarization ratio of the scattering phase function. The measurements of the physical properties of clouds and studies of their evolution during growth and dissipation should help in better understanding the radiative forcing that is still of much concern in climate change studies^{20,21}. The many different properties that can be simultaneously measured using a Raman lidar make it a most valuable tool for these investigations, and the three measurements that are most useful in studying the dynamical processes are the profile sequences of water vapor, aerosol optical extinction and temperature.

This paper briefly reviews the types of measurements that are made using Raman lidar to investigate the dynamical processes in the atmosphere; more complete descriptions of these lidar techniques are available³⁴⁻⁴². Brief descriptions of the primary measurement techniques used to obtain the profiles of water, temperature, and aerosol optical extinction are given in Section 2. Section 3 considers atmospheric stability as described by the adiabatic lapse rates of temperature and density, and by potential temperature profiles. Examples of each of several types of dynamical processes observed are then used, together with brief explanations, to illustrate atmospheric dynamics, including: convection cells, planetary waves, gravity waves, wind shear instabilities, nocturnal jets, turbulence cells, formation of an air pollution smog plumes, water vapor transfer into cumulous clouds, undular bore waves, and Brunt-Väisälä oscillations. Section 4 provides a short summary of our current capability and future goals for lidar to describe complex dynamical features.

2. LIDAR TECHNIQUES

An advantage of Raman lidar is that the molecular signature can be measured using any laser wavelength in the visible or ultraviolet wavelengths. Since the vibrational energy states are unique to a molecule, the wavelength of Raman shifted Stokes transition identifies the species present, and the intensity of the spectral line is used to calculate the concentration. The density concentration of each gas observed in the Raman scatter spectrum can be determined with three pieces of information that are normally available: (1) the laboratory measured cross-sections of the molecule, (2) the reference signal intensity of the molecule (O_2 , H_2O , CO_2 , O_3 , ...) as a ratio to the N_2 signal, and (3) the N_2 density profile calculated using the hydrostatic equation with inputs from the temperature profile measured by the same Raman lidar and the ground level measurements of pressure and temperature. The cross-sections for Raman scattering are small,

Stokes scattering is typically a factor of a thousand smaller than Rayleigh scattering, and the scattered photon is red-shifted and leaves an excited state molecule with a phonon. If the molecule should already exist in a higher vibrational level, the initial photon energy adds to the energy of the vibrational level and anti-Stokes scattering (blue-shifted) occurs. This unlikely case requires the molecule to already be in a vibrational state (tenths of an eV). The ranges Stokes and anti-Stokes vibrational Raman wavelength bands, which add to or subtract from the wavelength of the laser, are shown in Fig. 1 for the Nd:YAG laser fundamental and its harmonics. Raman scattering is another way, other than IR spectroscopy, to measure the vibrational and rotational spectra of molecules^{19,35,40,42}. An advantage of Raman lidar at UV is that the scattering cross-section is proportional to the frequency raised to the fourth power, and at the 4th harmonic, the 266 nm Raman spectrum is solar blind, which makes daytime measurements easier.

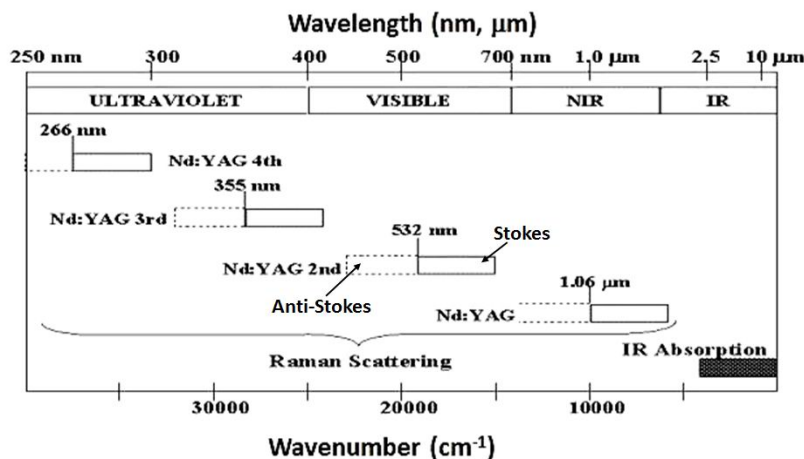


Figure 1. Wavelength bands in which Stokes and anti-Stokes vibrational Raman scatter signals can be observed are shown for the fundamental, 2nd, 3rd and 4th harmonics of the Nd:YAG laser. The IR Absorption region is the range of vibrational and rotational states, but this region is rotated 180° to represent the Stokes regions as indicated¹⁹.

Figure 2 shows a Raman lidar profile of water vapor compared with a simultaneous release of a rawinsonde balloon^{35,37}. The lidar profile has $\pm 1\sigma$ errors marked at the 75 m intervals, which correspond with the photon counting bin size of this instrument. At a few places along the profile, the two independent measurements diverge slightly, but this is not surprising, since the rising balloon drifts several kilometers away from the vertically pointed lidar. The relative intensities of the Raman scattered signals for a 2nd harmonic Nd:YAG laser at 532 nm are measured for species that are Raman active and have sufficient density. The signal for the H₂O (660 nm) is divided by the N₂ (607 nm) signal and multiplied by a factor to account for the PMT detector relative sensitivity, as well as by a factor determined from the published laboratory measurements of the Raman scatter cross-section for each molecule. These vibrational Raman signals of water vapor and molecular nitrogen are then used to calculate the water vapor mixing ratio at each range bin, and the statistical accuracy is determined.

The signal profiles from the rotational Raman bands at 530 nm and 528 nm are used to calculate the atmospheric temperature profile and $\pm 1\sigma$ statistical deviation shown in Fig. 3(a). The anti-Stokes bands used are indicated in a sketch in Fig. 3(b) for a 532 nm laser scattering in air^{35,37}. The anti-Stokes bands of rotational lines are preferred to remove the possibility of signal contamination from fluorescence. The rotational states are described by the Maxwell-Boltzmann distribution for a gas in thermal equilibrium, and changes in the shape of that distribution of rotational lines describe the changes in temperature. The measured ratios are used, together with the relative sensitivity of the two detectors (obtained by switching the input channels or using a standard source), to calculate the temperature profile. In this case, a three-point filter is used to smooth the curves. The measurements of atmospheric temperature from a rawinsonde balloon are also shown for comparison, and a few small acceptable departures are observed.

Raman lidar is particularly useful for describing the aerosol properties. Optical extinction includes contributions from both absorption by chemical species and scattering by molecules and particles. Over most of the visible spectrum, the extinction by absorption is a relatively small contribution to the total. The extinction by scattering and absorption by molecules is known to good accuracy from the measured or the modeled profiles. These contributions are removed to find the aerosol optical extinction. All of the Raman scatter profiles of the major molecular species can be used to calculate profiles of total optical extinction. The gradients in the measured molecular profiles at 607 nm (N₂), 530 nm

(rotational lines of $N_2 + O_2$) and 284 nm (N_2) are used to calculate the extinction profiles shown in Fig. 4²⁴⁻²⁸. The difference in slope from the expected gradient of the hydrostatic atmosphere and the measured gradient provide a direct measure of the total optical extinction. The total extinction value is then corrected by subtracting the absorption of gases from a model atmosphere and the scattering by the molecular atmosphere to find in the aerosol extinction profiles, see Fig. 4. The optical extinction profiles at several different wavelengths are used to describe changes in the particle size distribution, as a function of altitude. These measurements can then determine the visibility. The differences between the gradients in measured molecular profiles and the hydrostatic density profile gradient provide a direct measurement of the total optical extinction.

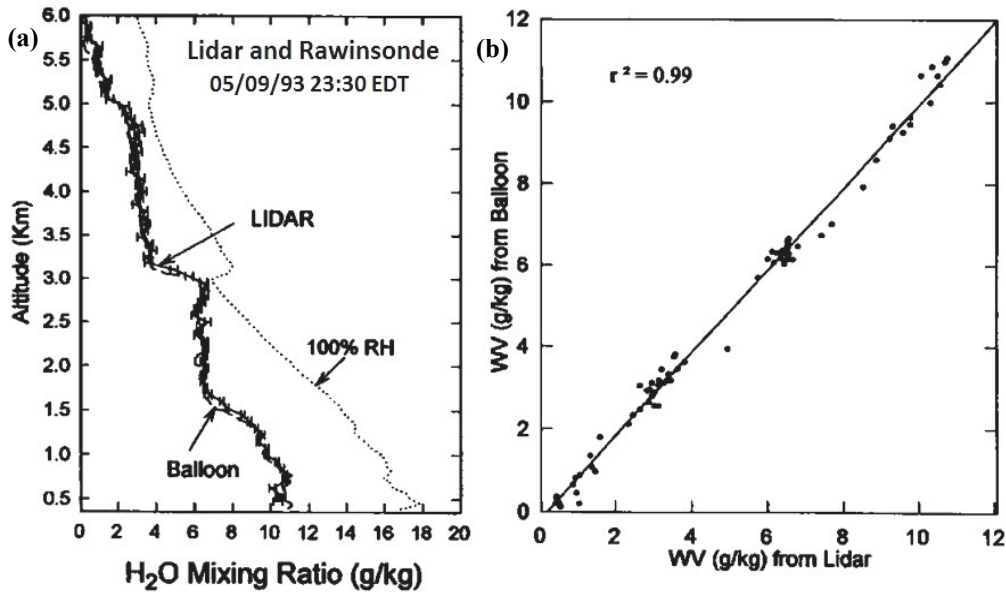


Figure 2. Raman lidar measurements of the water vapor mixing ratio compared with a rawinsonde balloon profile obtained simultaneously: (a) Vertical profiles of the lidar (75 m resolution) with $\pm 1 \sigma$ (statistical deviation) bars on the profile, (b) plot shows the correlation coefficient between the lidar and rawinsonde balloon measurements^{12,13,19,36-38}.

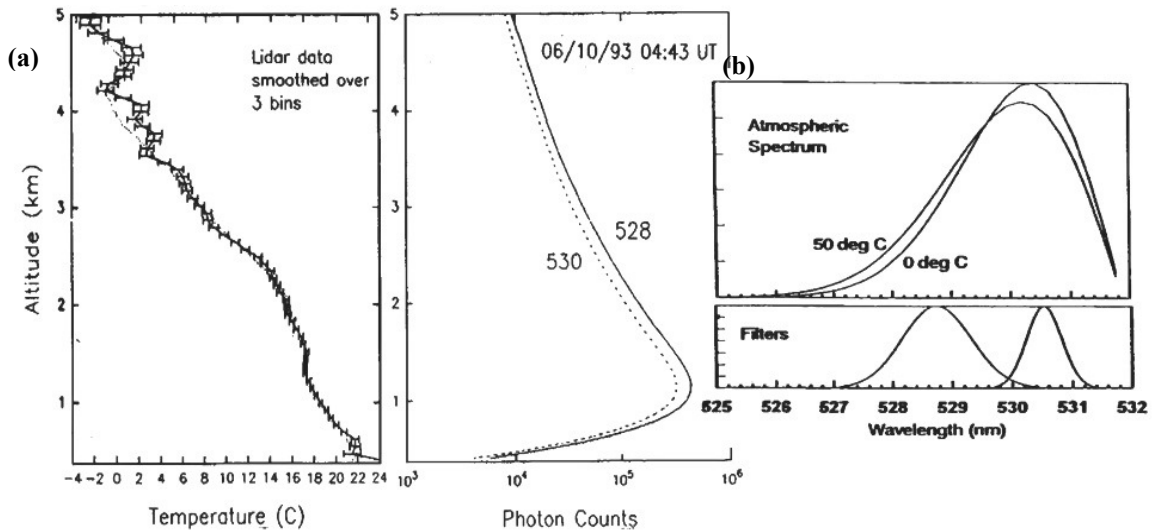


Figure 3. (a) Raman lidar temperature profile determined from the rotational Raman lines in two bands around 530 nm and 528 nm is compared with a simultaneous rawinsonde balloon, (b) temperature profiles calculated at 0°C and 50°C for the envelope of rotational lines are shown together with the bandpass filters used to calculate the temperature³⁶⁻³⁸.

The extinction profiles at 530, 607 and 284 nm measured in Philadelphia PA during NEOPS and in Hesperia CA during SCOS97 are shown in Fig. 4. The differences observed between the visible (530 nm and the 607 nm) profiles and the ultraviolet (284 nm) extinction are due to the large difference in size distributions of aerosols (the molecular absorption and scattering are removed)²⁴⁻²⁸. The large variation between these aerosol optical extinction profiles is due to the strong scattering dependence on the relationship between the scattering cross-section and the scattering wavelength. Figure 5 shows a graphical presentation of the relation between cross-section and particle size. The cross-section is proportional to the particle size, a , raised to the sixth power, $\sigma \sim a^6$, for $a < \lambda$, and squared, $\sigma \sim a^2$, for $a > \lambda$. In the region where the slope changes, between about $a/2 < \lambda < 5a$, the cross-section oscillates due to interference caused by diffraction around the particle, and refraction through it if the particle transmits at the wavelength. The profiles measured on the two dates in Fig. 4 show that the smaller particles usually dominate the particle population. The upper cloud layers at 4.5 and 5.4 km in Fig. 4(a) show the effects of multiple scattering, which results in whitening the spectrum and remove the wavelength dependence by scattering all wavelengths with the same efficiency. A similar effect can be observed in the surface layer.

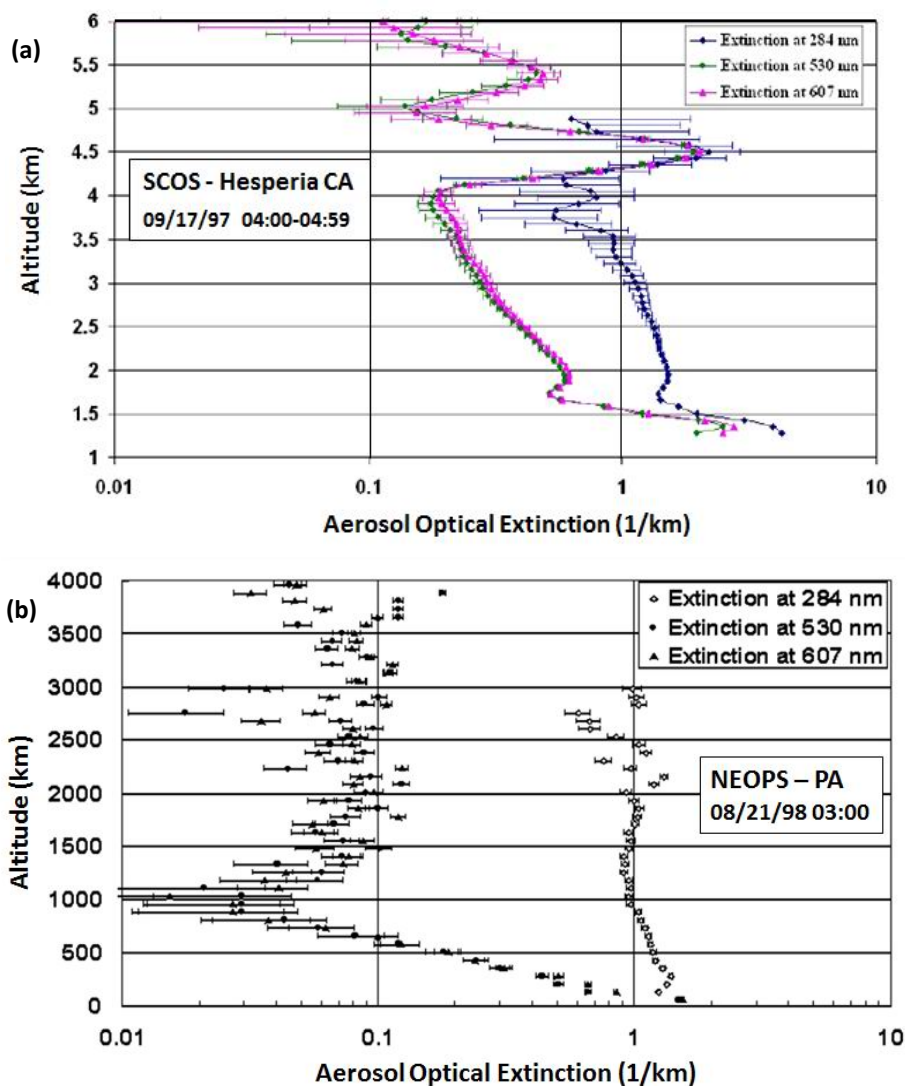


Figure 4. Aerosol optical extinction measurements, with $\pm 1\sigma$ statistical deviation, are derived from three profiles of the primary molecular species (284 nm, 503 nm and 607 nm); (a) SCOS97; (b) NARSTO-NEOPS^{24,25}.

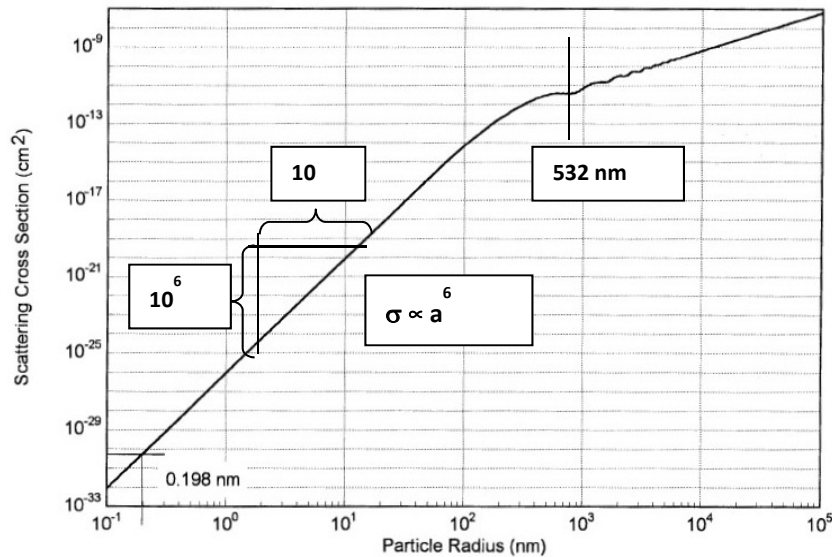


Figure 5. The scattering cross-section for spherical water particles is plotted versus particle radius for scattering by 2nd harmonic Nd:YAG laser (532 nm) by particles from the size of molecules to 100 μm , large rain drops. The oscillation when the particle size approaches the scattering wavelength is due to diffraction.

3. SIGNATURES OF ATMOSPHERIC DYNAMICS

The Raman lidar measurement of temperature can be used to determine the properties of atmospheric stability. The temperature adiabatic lapse rate of the atmosphere provides a way to describe atmospheric stability. For an adiabatic process, we can argue from the first law of thermodynamics that the equation, $C_p dT + g dz = 0$, must be valid in a dry and stable atmosphere, which is rearranged as, $dT/dz = g/C_p$, where $C_p = 1004 \text{ J/(kg } ^\circ\text{K)}$, the specific heat at constant pressure, and results in the dry adiabatic lapse rate of $\Gamma = -0.0098 \text{ K/m} = -9.8 \text{ } ^\circ\text{K/km}$. Temperature gradients that decrease more than $10 \text{ } ^\circ\text{K/km}$ are then dynamically unstable. Another way to examine the same property, the departure from hydrostatic equilibrium, is to examine the density gradient. The same stable condition occurs when the density gradient is less than the density adiabatic lapse rate, $\Gamma = -1/\rho (d\rho/dz) = g/C^2$ where the mass density is ρ and C is the speed of sound. If the density decreases less than about $10\text{-}13 \text{ } \%/ \text{km}$, the region will tend to be unstable^{2,3}. A range of values as a function of altitude is necessary because of the water vapor in the atmosphere. The moist adiabatic temperature lapse rate is $\sim 5.5 \text{ } ^\circ\text{K/km}$ in the troposphere, and the variation in the density adiabatic lapse rate is due to the changing speed of sound in a moist atmosphere. Another way to locate those less stable regions is to calculate the potential temperature profile. The potential temperature is the resulting temperature if an unsaturated parcel of air is moved adiabatically up or down to a pressure level of 1000 mb. By moving the parcel adiabatically, the slope of the profile provides a measure of the stability, somewhat like the temperature adiabatic lapse rate. Gravity waves are an interesting feature in the middle atmosphere, where they tend to grow to sufficient size to force the atmosphere into turbulence, which gradually transfers its energy as a turbulence cascade, Kolmogorov spectrum, toward the microscale limit, where it dissipates energy as temperature in the mesosphere or stratosphere. Wind shear instabilities also produce turbulence structures in regions of wind-shear layers, where the critical Richardson number is generally considered unstable at a small values, $Ri \leq 1/4$, but this will not be further discussed here, since the Raman lidar is not measuring the wind shear.

Sequential profile measurements of a Raman lidar provide a very useful picture to study atmospheric dynamic processes. The profiles of water vapor and aerosol distributions both provide tracers of dynamical motion, wind, convection, waves, and the presence of turbulence. The atmospheric stability is an important parameter for evaluating the sources and strength of turbulence in regions of the atmosphere. We can examine the stability using several parameters that are based on the lidar profiles of temperature and water vapor content; the temperature and density adiabatic lapse rates, and the potential temperature. Water vapor profiles and aerosol extinction profiles are also able to locate turbulent eddies and convection cells.

3.1 Tracers of Convection, Turbulence, and Aerosol Plumes

The time sequences of Raman lidar profiles provide a unique view of the dynamical process in an atmospheric volume. Figure 6(a) shows a 12-hour set of water vapor measurements from 8 AM (12:00 UTC) to 8 PM local time. These 1-minute profiles are stacked side-by-side and a 5-minute Hanning window has been applied to provide a picture of the atmosphere passing overhead. This presentation of the measured profiles provides an excellent way to observe the dynamical process active in the area, for example, the growth of the morning thermal convection cells that build to form the daytime boundary layer. An estimate of the size of the convective cells, as they move past the vertically pointed lidar in a light background wind, indicates that the cells are nearly circular. Growth of convective cells is observed on this clear morning, with a light wind across a large grassy field. Such uniform growth is only observed on a small fraction of the days. This particular day is special in another way; a moist air and pollution chemical layer was transported from power plants in the Ohio Valley in the fast moving nocturnal residual layer and mixed with the rising boundary layer over the site. When the residual layer and the boundary layer mix, we observe the appearance of turbulent eddies during the afternoon and evening. Photochemical processes generate smog and ozone layers during this afternoon period, as shown in Fig. 6(b). Both of these data sets are daytime measurements, which means that only the 4th harmonic of the Nd:YAG laser at 266 nm is used to take advantage of the solar blind background. After sunset and until sunrise, the higher power 2nd harmonic at 532 nm provides data to more than twice the altitude.

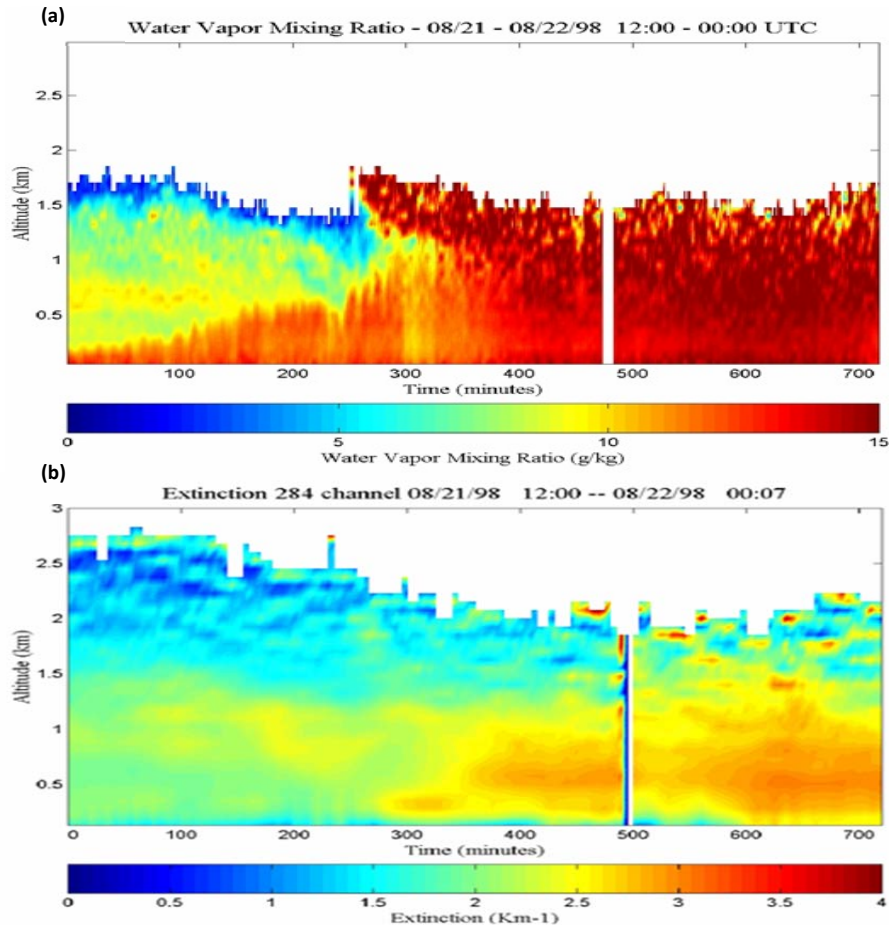


Figure 6. Measurements made at the NARSTO-NEOPS site in Philadelphia on 21 August 1998 between 8 AM and 8 PM local time show three interesting features of the dynamical processes active on that day; (a) morning convection cells grow to form the daytime boundary layer and then mixing downward of air transported in the residual layer to the region produce an air pollution event and initiated the observed turbulent eddies during the afternoon; (b) aerosol extinction profiles show the smog layer that developed from photochemical reactions^{19,38,39}.

3.2 Gravity Waves and Planetary Waves

Gravity waves launched from small pressure oscillations at low altitudes result in much larger features at higher altitudes as they propagate through the atmosphere, often without much dissipation of their energy until they grow sufficiently to become dynamically unstable and dissipate energy in turbulent heating. They are the primary heat source for the mesosphere; the warm winter mesosphere results from heating by energy dissipation of the strong waves launched in the winter, while blocking most of the wave spectrum by the meridional circulation pattern cools the summer^{4,6}. The several sets of rocket data are shown in Fig. 7(a). These include Super Loki Datasondes and Robin-Spheres, Viper Dart Spheres, and piezoelectric accelerometer spheres, launched during the MAPWINE project, and they show a large range gravity wave amplitudes, at times exhibiting >10% density amplitude fluctuation in the mesosphere. The data set also includes two profiles showing the effects when a phase overlap in planetary waves creates a density enhancement > 50% in the late winter³⁴. One particularly useful description for the scales of gravity waves to expect in the mesosphere, that shows the range of expected vertical and horizontal wavelengths and periods, is given by Hines¹, see Fig. 7(b).

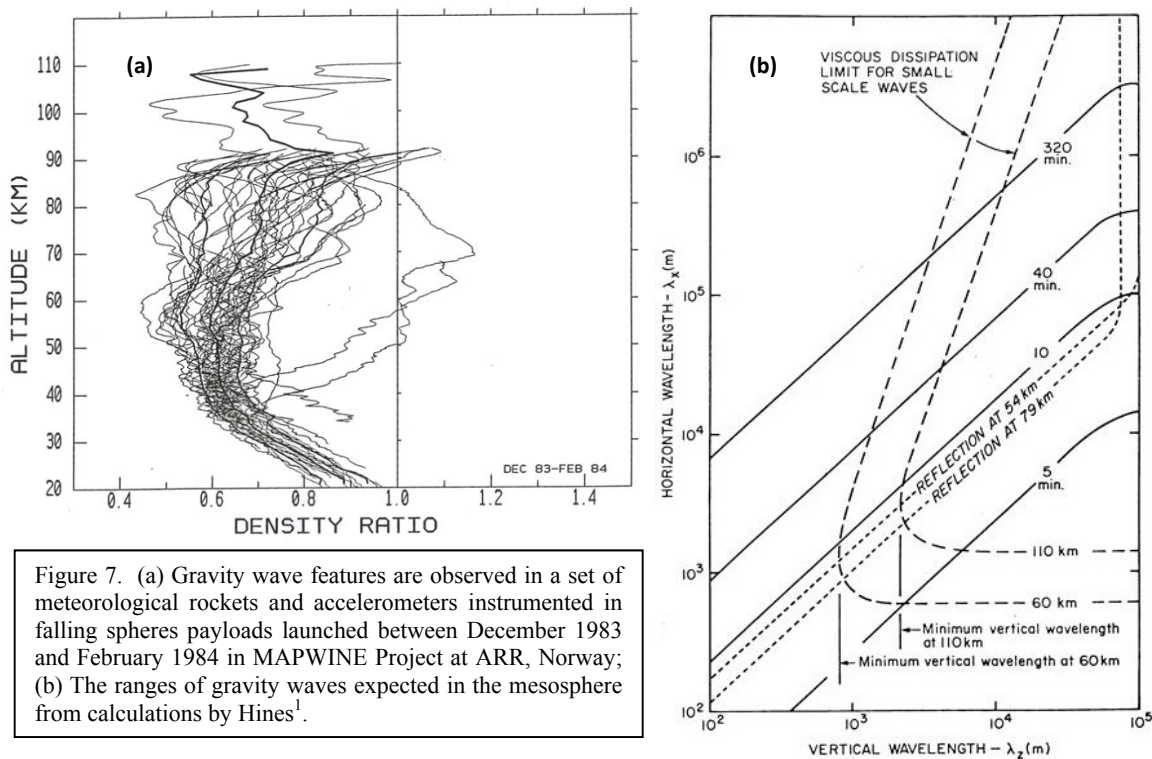


Figure 7. (a) Gravity wave features are observed in a set of meteorological rockets and accelerometers instrumented in falling spheres payloads launched between December 1983 and February 1984 in MAPWINE Project at ARR, Norway; (b) The ranges of gravity waves expected in the mesosphere from calculations by Hines¹.

Today, gravity wave studies are not limited to rocket probes, and may be viewed more continuously by using lidar techniques^{34,35,43,44}. Figure 8 shows an early study of gravity waves and planetary waves using a Rayleigh Lidar at Poker Flat research Range in Alaska during February 1986^{34,35}. At stratospheric and mesospheric altitudes, Rayleigh scatter from molecules in the aerosol-free atmosphere can be used to find the atmospheric temperature profiles by integrating the hydrostatic equation down the scattering profile^{2,3,34,35}. The density profiles are then found by tying to the relative density profile obtained from the measured temperature and the hydrostatic equation, to a measurement from a rawinsonde balloon at a low altitude overlap point to provide a corrected density profile. The density profiles measured on each of several evenings in February 1986 are shown as a ratio to the USSA76 Standard Model. Thin and persistent aerosol scattering layers at 26 km altitude, and others below, have not been corrected for the data set. The data set shows two periods, 19 February and 8 March, when a superposition of the planetary waves overlap to increase the density in the upper stratosphere, in one case by more than 50%. This process results in the adiabatic compressional heating of the lower stratosphere that increases the temperature, resulting in the event referred to as a “stratospheric warming.”

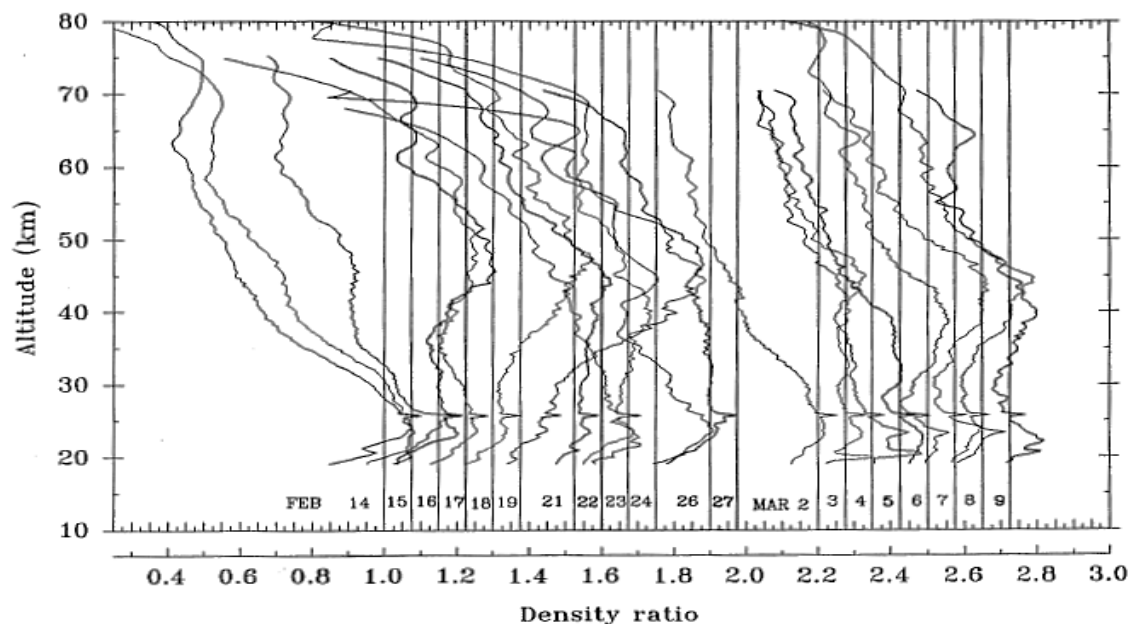


Figure 8. Rayleigh Lidar measured atmospheric temperature and density profiles on several of nights during February-March 1986 at Poker Flat Research Range, Alaska. This plot shows the increased density in the upper stratosphere that causes a warming in the lower stratosphere by adiabatic compression. On 19 February, the atmospheric density increased by >50% at 50 km compared to one-week earlier, and a second smaller event occurred on 7-8 March^{34,35}.

3.3 Low Level Jets and Sudden Convection Events

In regions where ridges and mountain slopes are found, the meteorological conditions at some distance away are often affected by the low level jets that form at night, when coupling to the surface is reduced. During the evening hours, the residual layer, a layer just above the nocturnal boundary layer, gains downslope momentum and is able to transport large air volumes over long distances. This transport is referred to as a low level jet, and it is an often occurring feature over a significant distance from the slopes of the Appalachian and Rocky Mountains. At the NEOPS field site in Philadelphia, the Low Level Jet was frequently observed by the Radar-RASS sounder operated there, see Fig. 9. The jet is particularly important in transferring the air from the region of power plants in the Ohio Valley to the Philadelphia area. The momentum of a jet is frequently coupled into the boundary layer atmosphere on the next day, and can deposit its air into the morning boundary layer, as either a sudden convection event, or by simply being mixed into the rising daytime boundary layer. The species transported into the area sometimes included PAN, which is a stable molecule at the temperatures a few hundred meters above the ground, but thermally decomposes to produce precursors for generating photochemical smog and ozone at the summer surface layer temperatures. The measurements in Fig. 9(a) show the wind velocity measured at the NEOPS site with a Doppler Radar-RASS instrument. The Low Level Jet observed in this case transports a dry air mass into the area, as seen in Fig. 6(b). Between 3AM and 7AM (sunrise), the jet replaces the air volume at altitudes between 400 and 700 meters.

An example of a sudden convection event that involved the transport of air pollution chemicals is shown in Fig. 10. The water vapor distribution does not exhibit the normal rising of the morning boundary layer, but shows sudden convection event at about 10AM. The convection penetrates into the air transported in the residual layer, and convection rapidly transports chemicals to the ground where they thermally decompose and produce the rather large amount of photochemical smog and ozone. When this sudden convection occurs, the air volume below 300 meters suddenly expands by a factor of three to five and thus dilutes the background concentration of ozone, until photochemical processes generate a much larger plume.

The features of the Low Level Jet and Sudden Convection Events are often observed in the data collected at the NEOPS site in Philadelphia during five summers of intensive field program activity. The Raman lidar is one of the few measurement tools available to enable observations for study of such events.

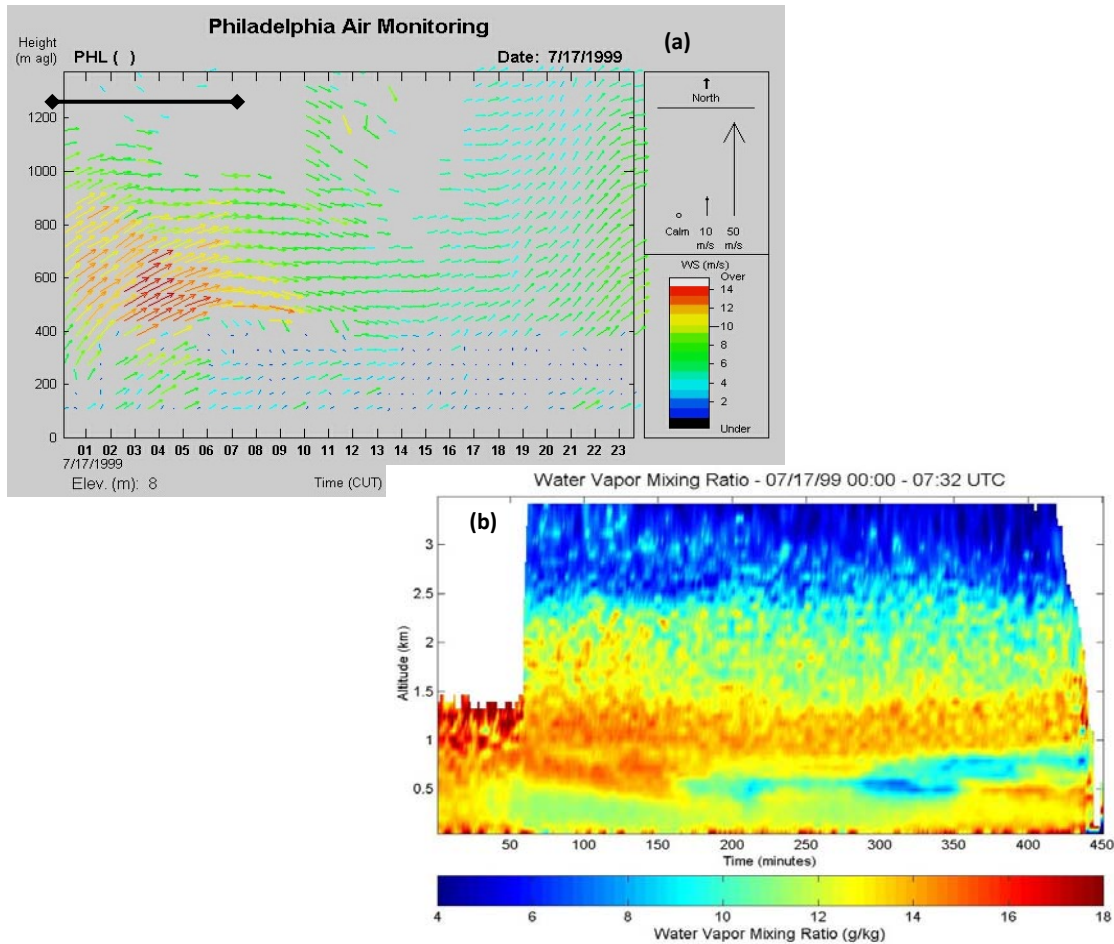


Figure 9. A low level jet is measured at the NEOPS field site in Philadelphia. (a) A 24-hr plot of the 30-min wind data on 17 July (bar indicates the period between midnight and 7:30 AM); (b) Changes in the boundary layer moisture occur in the altitude range (400-700 m) where the jet deposits a dry air mass between 3AM and 7AM⁴¹.

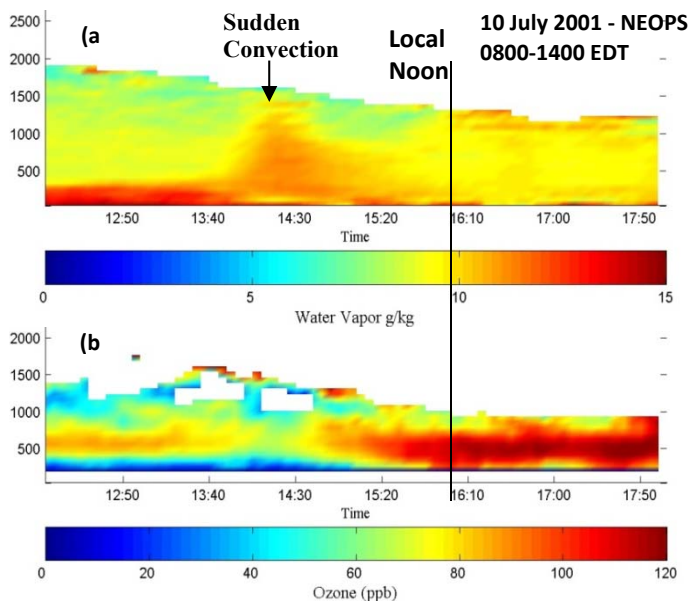


Figure 10. An example of a sudden convection event occurring about 10 AM local is seen in the water vapor tracer. The convection rises from ~300 m to 1500 m in about ½ hour. It appears to have rapidly mixed down chemicals from the residual layer, where the jet exists, to cause the air pollution event observed during the next several hours.

3.4 Special Dynamical Features: Bore Waves and Brunt-Vaisala Oscillations

One of the interesting surprises in measurements obtained at the NEOPS field site in Philadelphia is the observation of an undular bore wave that resulted from a strong low pressure front passing through the region. Figure 11 shows a 6-hr time sequence of water vapor profiles from 8 PM to 2 AM local time on 9 July 1999. The water vapor profiles are a useful tracer of the dynamics, when a cold front launches an undular bore wave as it passed over the field site. This undular bore wave has a 10.8 min oscillation, which is typical of the natural resonance frequency of the atmosphere.

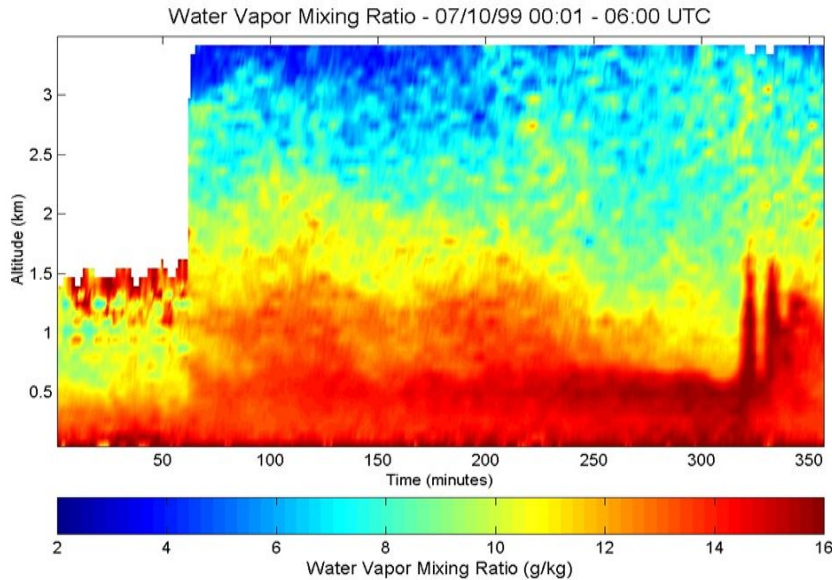


Figure 11. The water vapor mixing ratio profiles again serve as a dynamics tracer to observe an undular bore wave as a cold front proceeds through the area. This data shows that this oscillation period is 10.8 min. The disturbance reached the site at 1:20 AM local time on 10 July 1999 and was followed by rain and gusty winds.

Another interesting observation was made on the shore of the Arctic Ocean at Point Barrow AK on 27 May 1998 between 3 AM and 10 AM, see Fig. 12. The oscillation, ~ 10.5 min, was observed between 6-10 AM is at the natural resonance frequency, referred to as the Brunt-Väisälä frequency. This type of oscillation was observed on three different days near the end of May. Our conjecture is that these waves were most likely excited by the spring breakup of Arctic Ocean ice, when large pieces of ice collapsed into the sea.

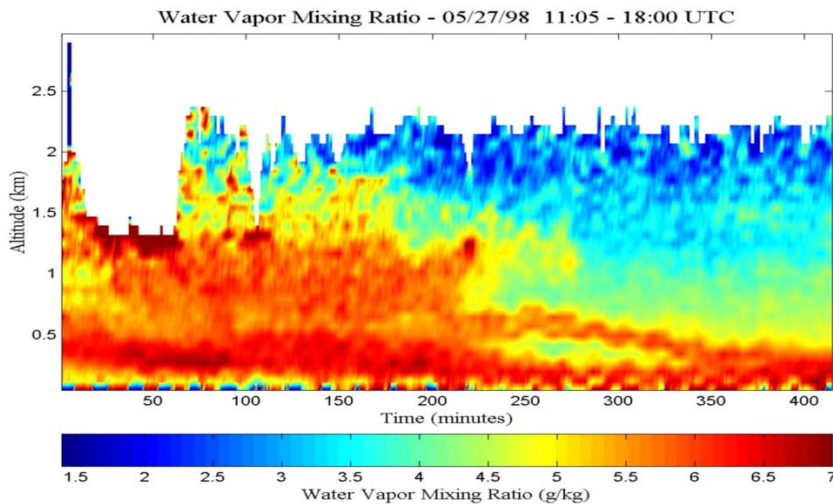


Figure 12. A buoyant oscillation forced at the Brunt-Väisälä frequency observed at Point Barrow Alaska on 27 May 1998 from 3-10 AM local time during the arctic springtime¹⁹.

3.5 Clouds and Microphysics Process

The sequences of water vapor, temperature and aerosol optical extinction profiles provide the opportunity to study the microphysical processes that occur as clouds evolve in time. Figure 13 shows the measured water vapor and temperature profiles and these are used to calculate the relative humidity. The humidity correlates well with the aerosol distribution measured at the same time. Measurements shown in Fig. 14 were obtained during a voyage of the USNS Sumner and show the way that clouds can grow rapidly by taking moisture directly from the water vapor in the marine layer.

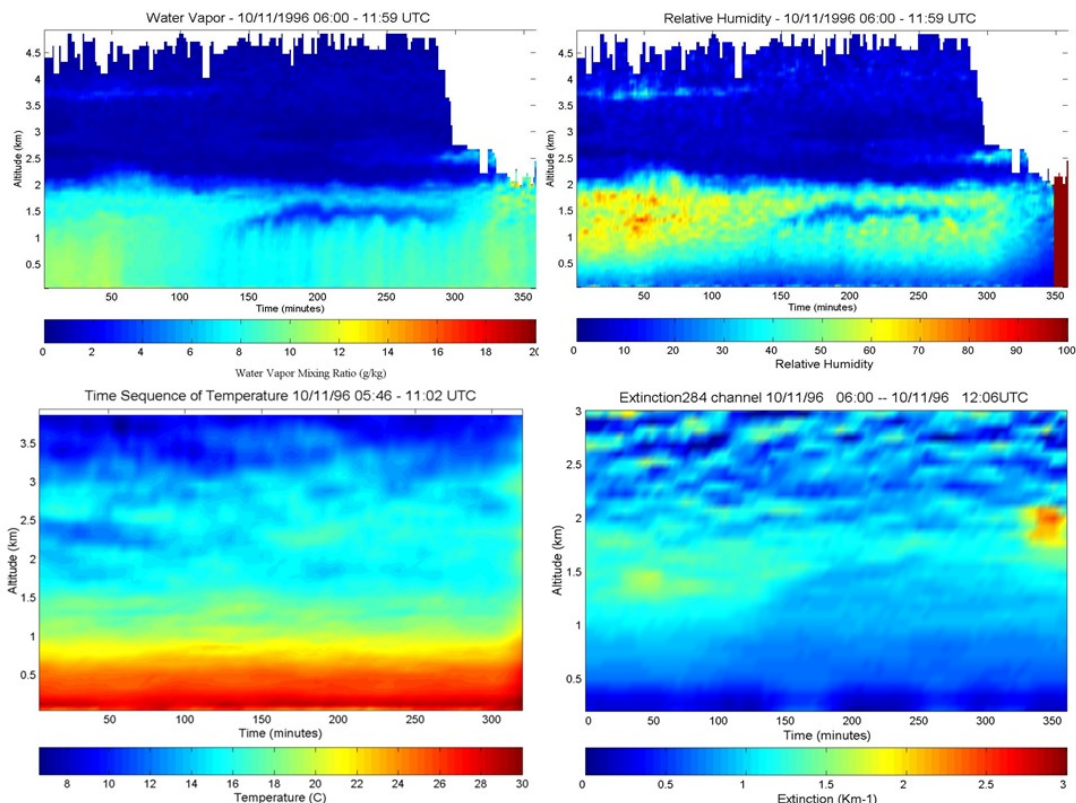


Figure 13. A six hour sequence of water vapor and temperature profiles are used to calculate relative humidity, which is compared with the UV optical extinction to observe the development of clouds^{12,42}.

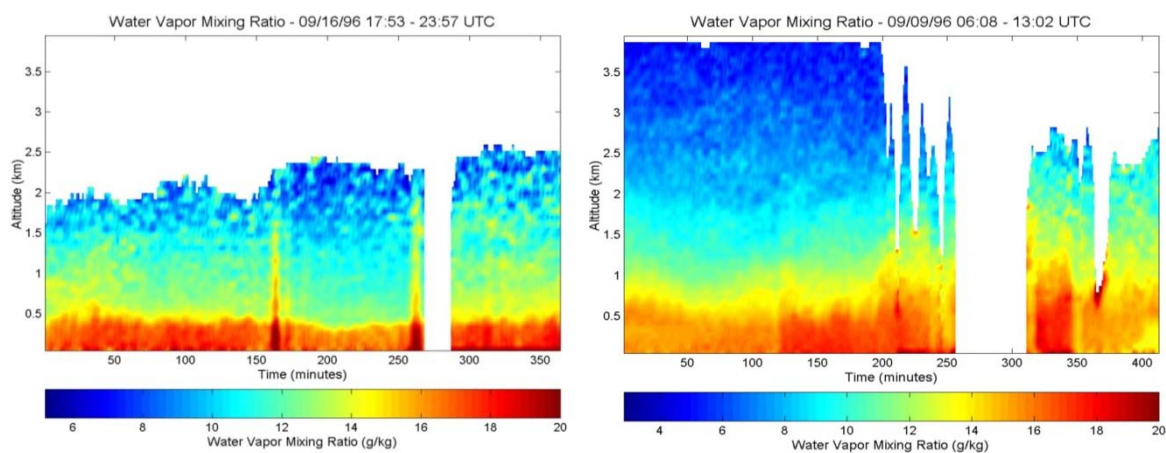


Figure 14. Water vapor can be transmitted directly into the base of clouds to rapidly grow those formed over the ocean by possibly using a heat engine effect to draw moisture from the marine layer into the cloud base¹⁹.

A data set obtained during the NARTSO-NEOPS campaign shows the time sequence plots of aerosol optical extinction at the ultraviolet and visible wavelengths on the night of 16 August, 1999 at the Philadelphia site during the NARSTO-NEOPS campaign, see Fig. 15. During this time period, we observe that several aerosol cloud layers advect through the laser beam, and our analysis of the ratio of the extinction coefficient of 530/284 shows the changes in particle size, both inside and surrounding the cloud layers. We also observed the variations in water vapor concentrations in and around the cloud regions at the same time. The 284 nm extinction profiles are most sensitive to the very small aerosols, the Aitken particles, and the 530 nm profiles are most sensitive to the accumulation mode particles. Both of these wavelengths are sensitive to the larger coarse mode particles which whiten the return in the central area of the clouds by multiple scattering, as was shown earlier in Fig. 4(a). Note that both data sets are plotted on the same scale to compare the in-cloud and out-of-cloud regions. Note that the small particles dominate the scattering outside the clouds. The technique does provide an interesting way to study the microphysical process in an evolving cloud.

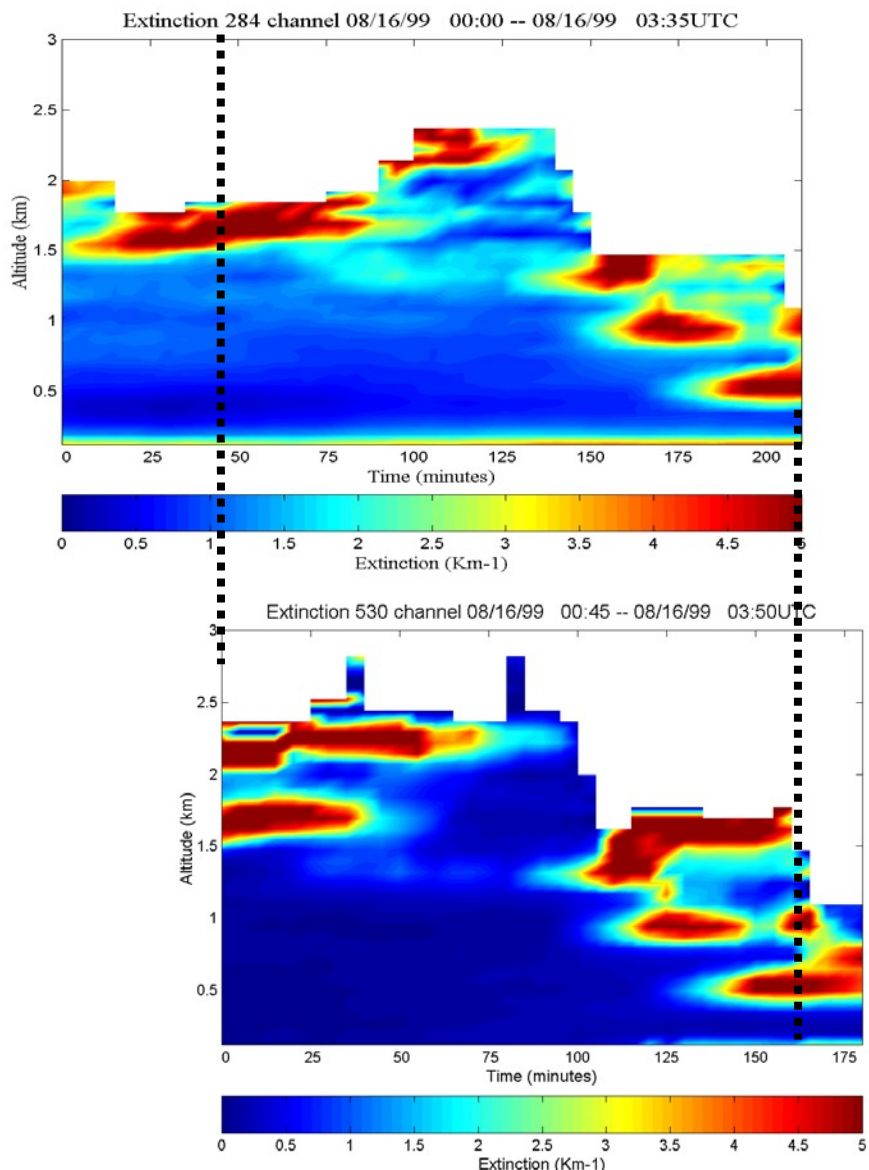


Figure 15. Aerosol optical extinction at UV and VIS wavelengths of several clouds moving through the vertical lidar beam show the changes in the size distribution of particles in and around the clouds^{20,21,42}.

4. SUMMARY

The goal of this study is to review a portion of a rather large data base of Raman lidar data to examine and show examples of the dynamical process operating in the atmosphere. It is quite challenging to observe the dynamics of the atmosphere using profiles of the important parameters obtained by using infrequent balloon instrument packages. The Raman lidar provides the opportunity to measure the profiles of temperature, water vapor and other properties continuously, in 1-min profiles, for periods of days. The same picture of the atmosphere painted with balloon payloads would require many thousands of releases. The Raman lidar technique for the primary measurements is introduced briefly for the parameters that can contribute best to the understanding of atmospheric dynamics; profiles of water vapor, temperature, and aerosol optical extinction. These are the ones selected to investigate dynamical processes associated with waves, convection, turbulence, and atmospheric stability. The two measurements also serve as tracers of atmospheric dynamics in the lower atmosphere; water vapor and aerosol extinction. Raman lidar measurements show examples of convection, turbulence, plumes, gravity waves, planetary waves, low level jets, sudden convection events, undular bores, Brunt-Väisälä oscillations, and examples of several observations of cloud dynamics. Among the interesting observations are the processes we call an undular bore and Brunt-Väisälä oscillations. These are related and differ in the source of the input energy to create the initial disturbance; both appear to be the natural resonance response of a pressure impulse on the atmosphere. Future investigations of atmospheric dynamics should benefit from the continued use of Raman Lidar to observe the tracers, which are water vapor and aerosols, and observe the phases of the water, sizes of the liquid and solid aerosols and their number density, as well as observe the properties of waves and turbulence in the atmosphere. Major benefits will be gained in the next generation of Raman lidar instruments by making use of higher speed electronics and improvements in lasers and detectors to allow spatial resolution of a meter and time resolution of a few seconds.

ACKNOWLEDGMENTS

The following organizations and individuals are acknowledged for their support and encouragement of lidar developments during the last 40 years at the Air Force Geophysics Laboratory, and then at Penn State University. The federal government has supported these instrument developments, several field campaigns, and shipboard tests that have been instrumental in carrying out this research, several of the major supporters have been: USAF Cambridge Research Laboratory (later Geophysics Laboratory), PSU Applied Research Lab, US Navy through SPAWAR Systems Division, PMW-185, NAVOCEANO, NAWC Point Mugu, and ONR, DOE, EPA (STAR Grant R826373), California Air Resource Board (SCOS), NASA, and NSF. The NARSTO-NEOPS air quality investigations were supported by USEPA STAR Grants with assistance from Pennsylvania DEP and MARAMA. Special appreciation goes to co-workers D. Sipler, G. Davidson, C. S. Gardner, U. vonZahn, D. Offermann, D. B. Lysak, F. Balsiger, T. M. Petach, J. Jenness, T. J. Kane, Z. Liu, D. M. Blood, and graduate students B. Chen, T. D. Stevens, P. A. T. Haris, M. D. O'Brien, D. Machuga, T. Manning, S. Sprague, G. OMarr, A. Achey, A. Nanduri, J. Park, C. Bas, J. Begnoche, R. Harris, P. J. Collier, T. Manning, G. Evanisko, S. Boone, G. Chadha, S. Unni, S. Kizhakkemadam, J. Collier, L. Liu, J. Yurack, G. O'Marr, S. Mathur, C. Slick, S. Sprague, A. Venkattarao, B. Mathason, S. Maruvada, D. Machuga, S. Rajan, *Savyasachee* Mathur, M. Zuger, G. Evanisko, J. Yurack, S. T. Esposito, K. Mulik, A. Achey, E. Novitsky, Y.-C. Rau, G. Li, S. Verghese, A. H. Willitsford, D. M. Brown, A. Wyant Brown, D. M. Edwards, M. Snyder for their outstanding technical contributions to these developments of the Raman lidar technology. The contributions of colleagues Rich Clark, S.T. Rao, George Allen, Bill Ryan, Bruce Doddridge, D. Killinger, Steve McDow, Delbert Eatough, Susan Weirman, Bart Croes, C. Richey, M. Thomas, S. V. Stearns, J. Lentz, Dennis Fitz are gratefully acknowledged.

REFERENCES

- [1] C.O. Hines, *The Upper Atmosphere in Motion*, *Am. Geophys. Union, Monograph* **18**, 1974.
- [2] C.R. Philbrick, E.A. Murphy, S.P. Zimmerman, E.T. Fletcher, Jr., and R.O. Olsen, "Mesospheric density variability," *Space Res.* **XX** (ed. M. J. Rycroft, Pergamon Press), pp. 79-82, 1980.
- [3] C.R. Philbrick, "Measurements of structural features in profiles of mesospheric density," in *Handbook for MAP* (Ed. S.K. Avery, SCOSTEP Secretariat, University of Illinois), **2**, pp. 330-340, 1981.
- [4] R.S. Lindzen, R.S., "Turbulence and stress owing to gravity wave and tidal breakdown," *J. Geophys. Res.* **86**, pp. 9707-9714, 1981.
- [5] D.C. Fritts, "Gravity wave saturation in the middle atmosphere: A review of theory and observation." *Rev. Geophys. Space Phys.* **22**, pp.275-308, 1984.

- [6] R.S. Lindzen, "Gravity waves in the mesosphere," in *Dynamics of the Middle Atmosphere* (Eds. J.R. Holton and T. Matsuno, D. Reidel Publ. Co.) pp. 3-18, 1984.
- [7] E.V. Thrane, O. Andreasen, T. Blix, B. Grandal, A. Brekke, C.R. Philbrick, F. Schmidlin, H.U. Widdel, U. VonZahn, and F.J. Luebken, "Neutral air turbulence in the upper atmosphere," *J. Atmos. Terr. Phys.* **47**, pp. 243-265, 1985.
- [8] C.O. Hines, "The generation of turbulence by atmospheric gravity waves," *J. Atmos. Sci.* **45**, pp. 1269-1278, 1988.
- [9] A.D. Fritts, S.A. Smith, B.B. Balsley, and C.R. Philbrick, "Evidence of gravity wave saturation and local turbulence production in the summer mesosphere and lower thermosphere during the STATE experiment," *J. Geophys. Res.* **93**, pp. 7015-7025, 1988.
- [10] C.R. Philbrick, J. Barnett, R. Gerndt, D. Offermann, W.R. Pendleton, Jr., P. Schlyter, J.F. Schmidlin, and G. Witt, "Temperature measurements during the CAMP program," *Adv. Space Res.*, **4**, 133-136, 1984.
- [11] C.R. Philbrick, D.P. Sipler, B.B. Balsley, and J.C. Ulwick, "The STATE experiment – mesospheric dynamics," *Adv. Space Res.*, **4**, pp. 129-132, 1984.
- [12] C.R. Philbrick, "Raman Lidar Characterization of the Meteorological, Electromagnetic, and Electro-optical Properties of the Atmosphere," in *Lidar Remote Sensing for Environmental Monitoring VI, Proc. SPIE 5887*, pp. 85-99, 2005.
- [13] C.R. Philbrick and K. Mulik, "Application of Raman Lidar to Air Quality Measurements," in *Conference on Laser Radar Technology and Applications, Proc. SPIE 4035*, pp. 22-33, 2000.
- [14] D.G. Murdock, S.V. Stearns, R.T. Lines, D. Lenz, D.M. Brown, and C.R. Philbrick, "Applications of Real-World Gas Detection: Airborne Natural Gas Emission Lidar (ANGEL) System," *J. Applied Remote Sensing*, **2**, 023518, 2008. DOI:10.1117/1.2937078
- [15] D.M. Brown, Z. Liu and C.R. Philbrick, "Supercontinuum lidar applications for measurements of atmospheric constituents" *Proc. SPIE 6950*, 69500B-1, 2008. DOI: 10.1117/12.778255
- [16] D.M. Brown, K. Shi, Z. Liu, and C.R. Philbrick, "Long-path supercontinuum absorption spectroscopy for measurement of atmospheric constituents," *Opt. Exp.* **16**(12), pp. 8457-8471, 2008.
- [17] P.S. Edwards, A.M. Wyant, D.M. Brown, Z. Liu, C.R. Philbrick, "Supercontinuum laser sensing of atmospheric constituents," *Proc. SPIE 7323*, 73230S 2009. DOI: 10.1117/12.818697
- [18] D.M. Brown, A.M. Brown, P.S. Edwards, Z. Liu; C.R. Philbrick, "Measurement of atmospheric oxygen using long-path supercontinuum absorption spectroscopy," *J. Appl. Remote Sens.* **8**(1), 083557, 2014. DOI: 10.1117/1.JRS.8.083557
- [19] C.R. Philbrick and H. Hallen, "Laser remote sensing of species concentrations and dynamical processes," in *Laser Radar Technology and Applications XIX, Proc. of SPIE 9080*, 90800Z, 2014. DOI: 10.1117/12.2050696
- [20] S.J. Verghese, A.H. Willitsford and C.R. Philbrick, "Raman Lidar Measurements of Aerosol Distribution and Cloud Properties," in *Lidar Remote Sensing for Environmental Monitoring, Proc. SPIE 5887*, pp.100-107, 2005.
- [21] Sachin J. Verghese, *Investigation of Aerosol and Cloud Properties Using Multi-wavelength Raman Lidar Measurements*, PhD Dissertation, Pennsylvania State University, Department of Electrical Engineering, 2008.
- [22] T.D. Stevens and C.R. Philbrick, "Atmospheric extinction from Raman lidar and a bi-static remote receiver," *Proc. IEEE Topical Symp. COMEAS* 10.1109, pp. 170-173, 1995.
- [23] Timothy D. Stevens, *Bistatic Lidar Measurements of Lower Tropospheric Aerosols*, PhD Dissertation, Pennsylvania State University, Department of Electrical Engineering, 1996.
- [24] G. Li, and C.R. Philbrick, "Lidar measurements of airborne particulate matter," in *Remote Sensing of the Atmosphere, Environment and Space, Proc. SPIE 4893*, 15, 2002.
- [25] G. Li, and C.R. Philbrick, "Study of airborne particulate matter using multi-wavelength Raman lidar," *Proc. 22nd ILRC, ESA SP-561*, pp. 377-380, 2004.
- [26] Edward J. Novitsky, *Multistatic Lidar Profile Measurements of Lower Tropospheric Aerosol and Particulate Matter*, PhD Dissertation, Pennsylvania State University, Department of Electrical Engineering, 2002.
- [27] E.J. Novitsky and C.R. Philbrick, "A Multistatic Receiver for Monitoring Lower Troposphere Aerosols and Particulate Matter," *Proc. 22nd ILRC, ESA SP-561*, pp. 219-222, 2004.
- [28] E.J. Novitsky and C.R. Philbrick, "Multistatic Lidar Profiling of Urban Atmospheric Aerosols," *J. Geophys. Res. Atmos.* **110**, D07S11, 2005.
- [29] A.M. Wyant, D.M. Brown, P.S. Edwards, and C.R. Philbrick, "Multi-wavelength, multi-angular lidar for aerosol characterization," in *Laser Radar Technology and Applications XIV, Proc. SPIE 7323*, 73230R-1-8, 2009. DOI: 10.1117/12.818686

- [30] A.M. Brown, M.G. Snyder, L. Brouwer, C.R. Philbrick, "Atmospheric aerosol characterization using multiwavelength multistatic light scattering," in *Laser Radar Technology and Applications XV*, Proc. SPIE **7684**, 76840I-1-11, 2010. DOI:10.1117/12.850080
- [31] Andrea M. Brown, *Multi-wavelength Multistatic Optical Scattering for Aerosol Characterization*, PhD Dissertation, Pennsylvania State University, Department of Electrical Engineering, 2010.
- [32] Anilkumar Nanduri, *Applications of an Acousto-Optic Tunable Filter in Remote Sensing*, Master's Degree Thesis, Pennsylvania State University, Department of Electrical Engineering, 1997.
- [33] Martin Chaplin, *Water Structure and Science*, web based publication viewed July 2015. http://www1.lsbu.ac.uk/water/water_structure_science.html
- [34] C.R. Philbrick, D.P. Sipler, B.E. Dix, G. Daivdson, W.P. Moskowitz, C. Trowbridge, R. Sluder, F.J. Schmidlin, L.D. Mendenhall, K.H. Bhavnani, and K.J. Hahn, *Measurements of the High Latitude Middle Atmosphere Properties Using LIDAR*, AFGL-TR-87-0053, 1987.
- [35] C.R. Philbrick and B. Chen, "Transmission of Gravity Waves and Planetary Waves in the Middle Atmosphere Based on Lidar and Rocket Measurements," *Adv. Space Res.* **12**, pp. 303-306, 1992.
- [36] C.R. Philbrick, "Raman Lidar Measurements of Atmospheric Properties," in *Atmospheric Propagation and Remote Sensing III*, SPIE **2222**, pp. 922-931, 1994.
- [37] C.R. Philbrick, D.B. Lysak, T.D. Stevens, P.A.T. Haris, and Y.-C. Rau, "Lidar Measurements of Middle Atmosphere Properties during the LADIMAS Campaign," *Proc. 11th ESA Symp.ESA*, **SP-355**, pp. 223-228, 1994.
- [38] S. Rajan, T.J. Kane, and C.R. Philbrick, "Multiple-wavelength Raman lidar measurements of atmospheric water vapor," *Geophys. Res. Let.* **21**, pp. 2499-2502, 1994.
- [39] K.R. Mulik and C.R. Philbrick, "Raman Lidar Measurements of Ozone During Pollution Events," in *Advances in Laser Remote Sensing, 20th ILRC*, Vichy France, pp. 443-446, 2001.
- [40] C.R. Philbrick, "Overview of Raman lidar techniques for air pollution measurements," *Proc. SPIE* **4484**, pp. 136-150, 2002.
- [41] C.R. Philbrick, "Application of Raman Lidar advancements in meteorology and air quality," in *Lidar Remote Sensing for Industry and Environment Monitoring III*, Proc. SPIE **4893**, pp. 61-69, 2003.
- [42] C.R. Philbrick, H. Hallen, A. Wyant, T. Wright, and M.G. Snyder, "Optical remote sensing techniques characterize the properties of atmospheric aerosols," in *Laser Radar Technology and applications XV*, Proc. SPIE **7684**, 76840J, 2010. DOI: 10.1117/12.850453
- [43] R.L. Collins and R.W. Smith, "Evidence of damping and overturning of gravity waves in the Arctic mesosphere: Na lidar and OH temperature observations," *J. Atmos. Solar-Terr. Phys.* **66**, pp. 867-879, 2004.
- [44] U. von Zahn, G. von Cossart, J. Fiedler, K.H. Fricke, G. Nelke, G. Baumgarten, D. Rees, A. Hauchecorne, and K. Adolfsen, "The ALOMAR Rayleigh/Mie/Raman lidar: objectives, configuration, and performance," *Ann. Geophys.*, **18**, pp. 815-833, 2000. DOI: 10.1007/s00585-000-0815-2